



Erdheim-Chester disease: diffusion-weighted imaging and dynamic contrast-enhanced MRI provide useful information

Thomas Van Den Berghe¹ · Esther Candries¹ · Nicolas Everaert¹ · Michael Saerens² · Jo Van Dorpe³ · Koenraad Verstraete¹

Received: 22 August 2022 / Revised: 9 December 2022 / Accepted: 12 December 2022 / Published online: 5 January 2023
© The Author(s), under exclusive licence to International Skeletal Society (ISS) 2023

Abstract

This is, to our knowledge, the first case report with in-depth analysis of bone marrow and bone lesions with diffusion-weighted imaging and dynamic contrast-enhanced MRI in Erdheim-Chester disease to date. We present a case of a 70-year-old woman who was referred for an X-ray of the pelvis, right femur and right knee after complaints of migratory arthralgia in hip and knee five months after an initial hip and knee trauma. Bone lesions on X-ray were identified. This case report highlights the strength and complementary use of modern multimodality multiparametric imaging techniques in the clinical radiological manifestations of Erdheim-Chester disease, in the differential diagnosis and in treatment response assessment, which is classically performed using ¹⁸F-FDG PET-CT. Erdheim-Chester disease is a rare form of non-Langerhans' cell histiocytosis, mainly affecting individuals in their fifth-seventh decade of life and without sex predominance. Apart from the typical bilateral symmetric lesions in long bone diaphyseal and metaphyseal regions and classically sparing the epiphyses, this multisystemic disease causes significant morbidity by infiltrating critical organs (the central nervous system, cardiovascular system, retroperitoneum, lungs and skin). With non-traumatic bone pain being the most common complaint, Erdheim-Chester disease is diagnosed most often in an incidental setting on imaging. The imaging workup classically consists of a multimodality approach using conventional radiography, CT, MRI, bone scintigraphy and ¹⁸F-FDG PET-CT. This case report extends this evaluation with diffusion-weighted imaging and dynamic contrast-enhanced imaging techniques.

Keywords Erdheim-Chester disease · Diffusion-weighted imaging · Dynamic contrast-enhanced MRI · X-ray · CT · SPECT · ¹⁸F-FDG PET-CT · Radiology · Imaging · Treatment response

Introduction

Erdheim-Chester disease (ECD) is a rare histiocytosis which can affect almost all organ systems [1, 2]. Recent molecular investigations have led to recognition of ECD as a neoplastic disorder, although the presence of an inflammatory environment is important in the pathogenesis and clinical manifestations [3, 4]. Typical findings include diabetes insipidus

of unknown origin, sclerotic bone lesions resulting in bone pain, restrictive pericarditis and retroperitoneal fibrosis [3]. Other possible affected systems include the skin and the nephrological, urological, respiratory, endocrine and central nervous systems [1, 2, 4, 5]. Current imaging recommendations for diagnosis and workout of patients with a suspected ECD include a CT chest, abdomen and pelvis, an ¹⁸F-fluorodeoxyglucose (FDG)-PET-CT including the head and distal extremities and an MRI of the brain and the heart [3]. Yet, the gold standard for diagnosis is histopathologic examination of a suspicious bone or soft tissue lesion, which may be challenging. Classic histopathologic features include foamy or lipid-laden histiocytes surrounded by fibrosis and Touton giant cells. The histiocytes typically show CD68, CD163 and factor XIIIa positivity with langerin and CD1a negativity [3]. Additionally, molecular analysis exploring mutations in the MAPK pathway (*BRAF*, *KRAS*, *NRAS*, *MAP2K1*, *ARAF*), which are present in > 80% of patients, is

✉ Thomas Van Den Berghe
thovdnbe.VanDenBerghe@ugent.be;
thomasdanae@hotmail.com

¹ Department of Radiology, Ghent University Hospital and Ghent University, Ghent, Belgium

² Department of Oncology, Ghent University Hospital and Ghent University, Ghent, Belgium

³ Department of Pathology, Ghent University Hospital and Ghent University, Ghent, Belgium

mandatory as they support the diagnosis even in the absence of typical histopathological features and form a potential treatment strategy [3, 6]. Treatment with *BRAF* and/or *MEK* inhibitors is often successful and secondary resistance is extremely rare [1, 3]. There are no prospectively validated response criteria for ECD. Follow-up with ^{18}F -FDG-PET-CT every three to six months, which exposes the patient to a high dose of ionizing radiation, is recommended. Multiparametric magnetic resonance imaging (MRI) with functional MRI sequences consisting of diffusion-weighted imaging (DWI) and dynamic contrast-enhanced (DCE)-MRI may be a valuable alternative, as this reduces ionizing radiation and may reflect tissue biology more accurately. We report a case of ECD with *BRAF V600* mutation, treated with *BRAF*-*MEK* inhibitors (dabrafenib and trametinib), with longitudinal follow-up with DWI and DCE-MRI, which may provide new insights into lesion characteristics and tumor biology at diagnosis and during treatment regarding cellularity, water diffusion capacity, and vascularization.

Case report

Initial presentation

A 70-year-old woman was referred to the hospital for an X-ray of the pelvis, right femur and right knee after complaints of migratory arthralgia in hip and knee five months after an initial hip and knee trauma. The patient initially reported pain in the right hip, groin, thigh and knee. No further attention was paid to these complaints by the patient as she attributed them to age-related degeneration. The personal medical history shows a diagnosis of systemic lupus erythematosus, diabetes insipidus suspected to be linked to the systemic lupus, arterial hypertension and recurrent syncope. There is a familial history of multiple sclerosis and malignancy of the colon and the brain.

Imaging

X-rays of the pelvis, right femur, and right knee were performed to investigate possible causes of the reported migratory arthralgia. Two osteolytic lesions were detected in the right distal femur and in the medial aspect of the lesser trochanter of the right proximal femur, which were initially suspected to be incidentally detected bone metastases. Both lesions were radiolucent, irregular and ill defined. No cortical destruction or soft tissue mass was observed. No other abnormalities could be observed (Fig. 1a–c).

A thorough workup for metastasis of a solid tumor or multiple myeloma (MM) was initiated. Lab analysis showed normal renal and hepatic function. Free light chains kappa and lambda were raised (32.20 mg/l and 36.94 mg/l,

respectively), as well as the IgM and IgG fractions (16.35 g/l and 2.42 g/l, respectively). Immunofixation showed a vague and small band in the lambda fraction. Upon bone marrow biopsy, there was no clonal expansion of plasma cells. As such, a diagnosis of MM was highly unlikely. Moreover, no primary tumor was detected with mammography, breast and thyroid ultrasound, gastrointestinal endoscopy and chest and abdominal CT. She was then referred to our tertiary hospital for further examination. In order to characterize the osteolytic lesions, the chest and abdominal CT were re-evaluated (Fig. 1d–j). We found extensive, irregular bone lesions suspected for malignancy. Most lesions were osteolytic and had heterogenous sclerotic margins. Some cortical thickening was visible around the lesions, especially in the iliac bone. The lesions in the right and left iliac bone also showed cortical breakthrough with associated soft tissue masses. Similar lesions were detected in the right femur, right scapula and axillary part of the seventh left rib, without cortical breakthrough. No lesions were observed in the spine.

Late whole-body scintigraphy images with attenuation correction (IRACRR) showed increased uptake in the cranial and distal parts of the right femoral diaphysis, the cranial part of the left and right tibial diaphysis, the right sacroiliac joint, right scapula, axillary part of the ribs, right humeral head and the right mandible. Late tomography images showed increased uptake in the cranial and distal parts of the right femoral diaphysis, the left femoral diaphysis, the cranial part of both tibial diaphyses, both sacroiliac joints and the transition of the L5-S1 facet joints on the right side, suspected for malignancy. For the lesion in the right mandible, a differential diagnosis of osteonecrosis could not be excluded.

An ^{18}F -FDG-PET-CT examination (Fig. 2) was performed to identify a possible primary tumor. The PET-images were corrected for tissue attenuation using CT (attenuation correction with low mAs and 120 kV). High FDG uptake was seen in the right inferior border of the mandible, the gastroduodenal transition, both sacroiliac joints, the left iliac bone, the cranial and distal parts of the right femoral diaphysis, the right scapula and humeral head, and the axillary part of the seventh left rib. The whole-body CT images matched the images made prior, with the addition of an osteolytic lesion in the ascending ramus and corpus of the right mandible. The bone lesions were suspected for bone metastases, except for the lesion in the mandible, which could also be an osteonecrotic lesion. Gastroscopy with biopsy was performed to evaluate the gastroduodenal transition. No primary tumor could be identified.

A 1.5 Tesla whole-body MRI (Siemens Avanto Fit, Siemens Healthineers, Erlangen, Germany) was performed to investigate the detected osteolytic lesions and potential differential diagnoses like metastases and plasma cell dyscrasias. The protocol consisted of whole-body coronal



Fig. 1 X-rays of the right knee and hip (a–c) and CT thorax and abdomen in bone window (d–j). **a, b** Coronal and sagittal views of the knee joint reveal an osteolytic lesion in the distal third of the femur (arrow). **c** Coronal view of the hip joint and proximal femur reveals an osteolytic lesion in the medial aspect of the lesser tro-

chanter (arrow). Coronal (d, e, j), sagittal (f–h) and axial (i) views show multiple osteolytic lesions (arrows) of the right and left iliac bone, right femur, right scapula and axillary part of the seventh left rib without and with (circle) cortical breakthrough and associated soft tissue masses

T1- and T2-STIR-weighted images and sagittal T1-weighted, T2-weighted with fat saturation and contrast-enhanced T1-weighted images with fat saturation, DWI, and DCE-MRI of the thoracic and lumbar spine and sacrum (Table 1). Focal bone marrow lesions were detected in the entire axial and appendicular skeleton, except for the left scapula [7] (Fig. 3). The lesions' diameters varied from 3 mm (left humerus) to 63 mm (right posterior iliac bone). Other extensive lesions were detected in the distal lateral metaphysis of

the right femur (52 mm), the right lesser trochanter (41 mm), the right scapula (33 mm), the right humerus (20 mm), the posterior aspect of the left seventh rib (10 mm) and the mandible (9 mm). They were characterized by a low signal intensity (SI) on T1-weighted images and an intermediate to high SI on T2-weighted images with fat saturation and extensive enhancement. Furthermore, the lesions were inhomogeneous with irregular borders and showed central fat inclusions. These changes were visible both on the coronal

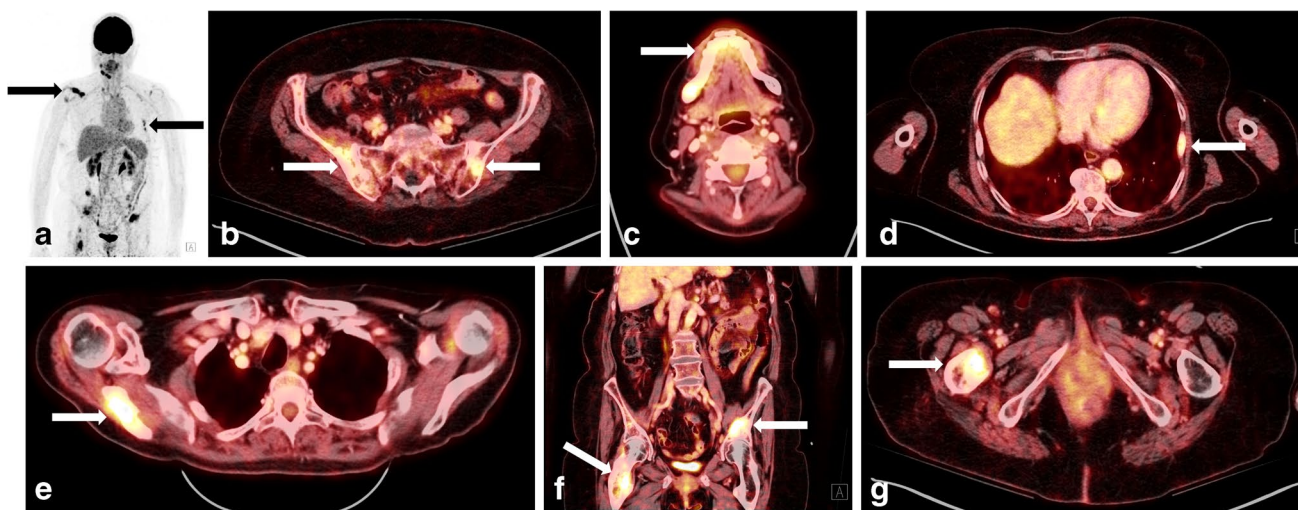


Fig. 2 Axial (b, c, d, e, g) and coronal (a, f) whole-body ^{18}F -FDG-PET-CT images show increased non-physiological uptake in the right inferior border of the mandibular ramus, the gastroduodenal transi-

tion, both sacroiliac joints, the base of the left iliac bone, the cranial part of the right femur, the right scapula and humeral head and the axillary part of the seventh left rib (arrows)

and the sagittal images. The bone marrow surrounding the lesions in the spine and elsewhere in the skeleton appeared normal. The lesions presented with diffusion restriction on the DWI sequences (Fig. 4b, c) and showed highly increased vascularization and perfusion on DCE-MRI (Fig. 4d). The surrounding bone marrow showed no diffusion restriction and normal, slow time-intensity curves [8]. No increased vascularization and perfusion were noted.

A DCE-MRI of the thoracic and lumbar spine was performed in the sagittal plane (7.5 ml Gadovist bolus, arrival time 7.14 s, 20 ml saline flush). Qualitative, semi-quantitative and quantitative analyses were performed using an additional postprocessing pipeline (Siemens Syngo.Via VB60A_HF01, Siemens Healthineers, Erlangen, Germany). For the qualitative analysis, regions of interest were drawn in the L3 and S3 lesions, in the paravertebral muscles, in the aorta and in the T10 and L4 vertebral bodies and time-intensity curves (TIC) were calculated. The aorta showed a typical arterial type IV TIC with a quick enhancement, steep wash-in followed by a wash-out, indicating good quality of the contrast injection [8]. The paravertebral muscles showed a typical type II curve with a slow wash-in, higher amplitude and slow sustained enhancement. T10 showed a type II curve with a low maximal enhancement, a slow enhancement, slow wash-in and sustained enhancement, indicating low perfusion and tissue vascularization, high capillary resistance and low capillary permeability [8]. L4 showed a type I curve with almost no enhancement. The lesion in L3 showed an active type IV curve with steep first pass, rapid wash-in, maximal enhancement higher than that in the aorta and strong wash-out, indicating very high perfusion, minimal vascular resistance and small interstitial space [8].

The lesion in S3 showed a type III curve with a steep first pass, rapid wash-in and plateau phase but with a very slow wash-out, indicating higher capillary resistance [8] (Fig. 4d).

Additionally, a semi-quantitative analysis was performed to derive the TIC parameters of the previously used regions of interest. A constant T1 protocol was used. Parameters included wash-in, wash-out, time-to-peak, the positive enhancement integral and the initial area under the curve (iAUC) (Table 2). A quantitative analysis was performed to generate the time-concentration curve to derive the characteristic parameters describing the contrast distribution over the vascular, interstitial and cellular compartments. The Tofts pharmacodynamic model was applied to calculate K_{trans} , K_{ep} , volume of the extracellular extravascular space (V_e) and iAUC [9] (Table 2). A pixelwise T1 protocol and slow arterial input function type (chi-square = 0.033) were used.

Anatomopathological and laboratory investigation

A bone biopsy of the right posterior superior iliac spine was conducted to investigate one of the detected bone lesions suspected for malignancy (Fig. 5). The bone marrow could be investigated for a variety of differential diagnoses like MM, Langerhans cell histiocytosis or lymphoma at the same time. A control CT pelvis was conducted to evaluate the biopsy trajectory and rule out possible sampling error.

The biopsy underwent decalcification prior to microscopic investigation. Bone trabeculae interspersed with hematopoietic tissue were evident. The bone marrow had a normal cellularity. All hematopoietic lineages were well represented and showed normal maturation. Several large areas

Table 1 Imaging parameters of the whole-body MRI examination with whole-body sagittal and coronal anatomical sequences, sagittal spine diffusion-weighted imaging and sagittal spine dynamic contrast-enhanced imaging

	WBT1sag (TSE)	WBT2FSsag (TSE)	WBT1FS- sag + Gd (TSE)	WBT1cor (TSE)	WBT2cor (TIRM)	SpineDWIsag (3 scan trace)	SpineT- 1vibesag pre-dynamic	SpineT1twist- DCEsag
Echo time (ms)	10	68	10	8.8	108	86	1.59	1.73
Repetition time (ms)	654	3470	516	661	8640	5100	5.37	4.25
Inversion time (ms)	N/A	N/A	N/A	N/A	140	180	N/A	N/A
Slice thick- ness (mm)	3.3	3.3	3.3	7	7	3	4	4
Spacing (mm)	3.3	3.3	3.3	7	7	3.3	N/A	N/A
Scanning sequence	SE	SE	SE	SE	SE/IR	EP/IR	GR	GR
Sequence variant	SK/SP/OSP	SK/SP/OSP	SK/SP/OSP	SK/SP	SK/SP/MP (scan option IR)	SK/SP/MP/ OSP (scan options IR/ PFP/FS)	SP/OSP	SP/OSP
Acquisition type	2D	2D	2D	2D	2D	2D	3D	3D
b-values	N/A	N/A	N/A	N/A	N/A	b0, b200, b400, b600, b1000	N/A	N/A
Number of averages	2	1	2	3	1	3	8	1
Magnetic field strength (Tesla)	1.5	1.5	1.5	1.5	1.5	1.5	1.5	1.5
Number of phase encoding steps	576	767	576	384	383	179	189	173
Echo train length	3	13	3	3	21	89	1	0
Transmit coil	Body	Body	Body	Body	Body	Body	Body	Body
Acquisition matrix	N/A	N/A	N/A	0/384/384/0	0/384/384/0	0/192/192/0	0/192/146/0	0/192/138/0
Flip angle (degrees)	150	150	150	150	150	90	2 and 15	12
Pixel spacing	0.91/0.91	0.91/0.91	0.91/0.91	1.30/1.30	1.30/1.30	1.67/1.67	2.34/2.34	2.34/2.34
Field of view	350×782	350×782	350×782	500×1279	501×1285	319×319	450×450	450×450
Contrast medium used	N/A	N/A	Gadovist (gadobutrol)	N/A	N/A	N/A	N/A	Gadovist (gadobutrol)
Contrast vol- ume (cc)	N/A	N/A	7.5	N/A	N/A	N/A	N/A	7.5
Temporal resolution	N/A	N/A	N/A	N/A	N/A	N/A	N/A	1 image/1.5 s (acquisition time 117.5 s)

2D two-dimensional, 3D three-dimensional, *b* diffusion-sensitizing gradient, *cor* coronal, *cc* cubic centimeter (milliliter), *DCE* dynamic contrast-enhanced (MRI), *DWI* diffusion-weighted imaging, *EP* echo planar, *FS* fat saturated, *Gd* gadolinium, *GR* gradient recalled, *IR* inversion recovery, *mm* millimeters, *MP* MAG prepared, *ms* milliseconds, *N/A* not available, *PFP* partial Fourier phase, *sag* sagittal, *SE* spin echo, *SK* segmented k-space, *SP* spoiled, *OSP* oversampling phase, *T1* T1-weighted imaging, *T2* T2-weighted imaging, *TIRM* turbo inversion recovery magnitude, *TSE* turbo spin echo, *WB* whole-body

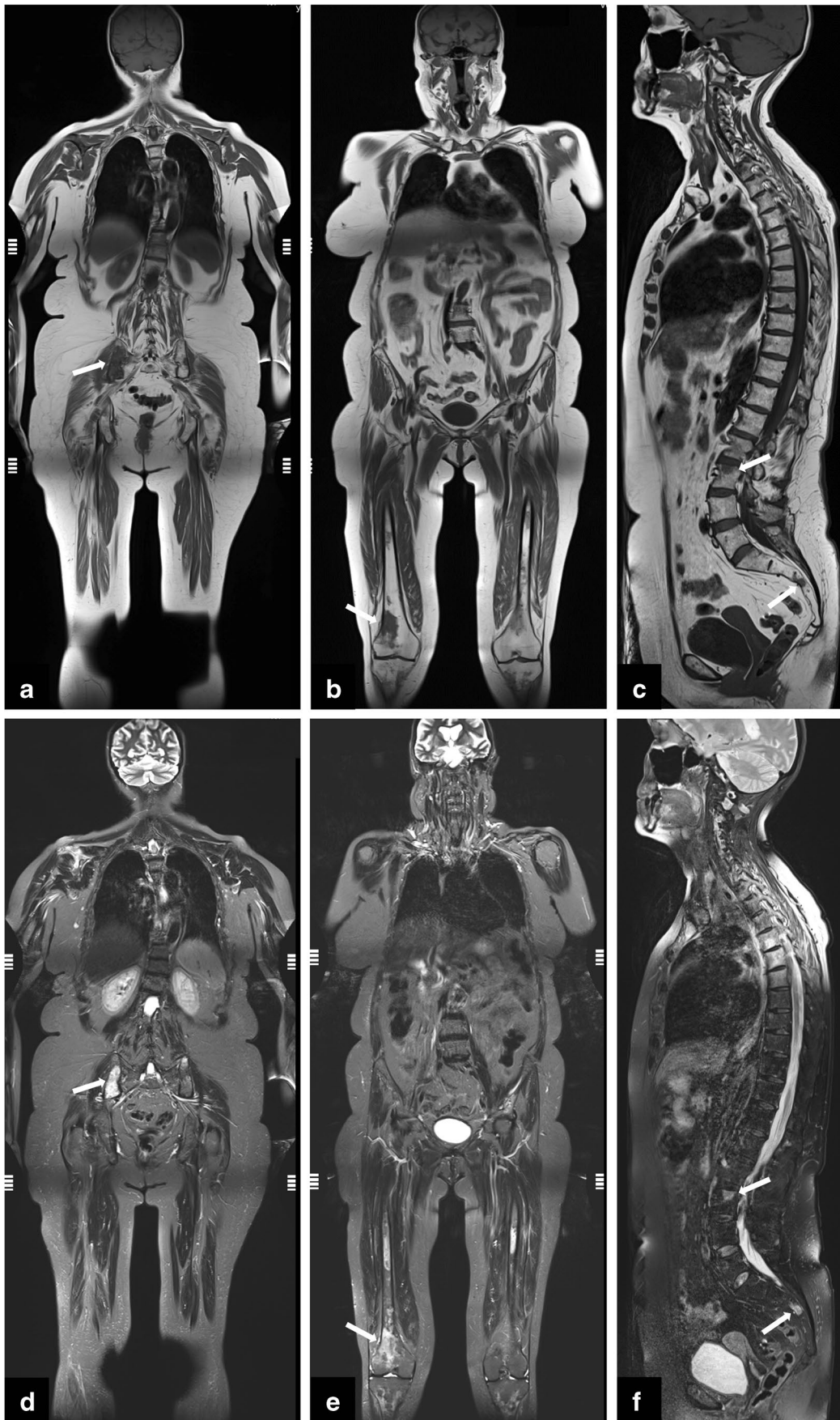


Fig. 3 Whole-body MRI examination with T1-weighted (upper row) and T2-weighted images after fat saturation (lower row). **a, d** Coronal images show a large T1 hypo- and T2-STIR hyperintense lesion of the right iliac bone with irregular borders (arrow). **b, e** Coronal images show a large T1 hypo- and T2-STIR hyperintense lesion of the distal right femur with irregular borders (arrow). **c, f** Sagittal images show two large T1 hypo- and T2-STIR hyperintense lesions of the L3 and S3 vertebral bodies (arrows)

of fibrosis were present in the bone marrow, which demonstrated focal lymphocytic infiltrates and scattered plasma cells. At high magnification, some histiocytes with ill-defined vacuolated cytoplasm could be discerned in the areas of fibrosis. Immunohistochemistry (IHC) of the lymphoid infiltrates showed both CD3 and CD20 positivities, indicating the presence of both B- and T-lymphocytes. No atypical lymphocytes could be identified. IHC for CD138 confirmed increased plasma cells, polytypical for kappa and lambda light chains. In MM, a monoclonal expansion of kappa or lambda plasma cells would be expected [10]. Plasma cells were mainly positive for IgG without increase of IgG4-expressing cells, indicating the lesions were not caused by IgG4-related disease. No aberrant expression of cytokeratins or CD30 was seen, excluding metastatic malignant epithelial cells and anaplastic large cell or Hodgkin lymphoma, respectively. IHC for CD68 demonstrated multiple histiocytes. These did not stain for CD1 and langerin, excluding Langerhans cell histiocytosis [5]. A slight increase of mast cells was noted in the fibrotic areas by IHC for CD117 and mast cell tryptase. There was, however, no cluster formation and the mast cells showed normal morphology, making the diagnosis of a mast cell tumor unlikely. ALK, HMB45 and S100 IHC were negative, making the diagnosis of anaplastic large cell lymphoma and melanoma unlikely as well. Additionally, S100 negativity again pointed toward ECD, as this is usually positive in a Langerhans cell histiocytosis [5]. The blood vessels were ERG-, CD34- and CD31-positive, indicating normal presence of endothelial cells and possible endothelial progenitors caused by angiogenesis.

The *BRAF* mutation test detected a *V600E/E2/D* mutation in codon 600 of *BRAF* (Idylla™ *BRAF* Mutation Test), which supported the diagnosis of ECD [3, 6].

A new biopsy of the right iliac crest confirmed the diagnosis, demonstrating the same morphological and immunohistochemical findings.

Evolution

The patient was hospitalized for additional investigations in the workout of ECD. The osteolytic lesions and diabetes insipidus of the patient were deemed to fit the diagnosis of ECD [3]. The patient was referred to dermatology and ophthalmology and underwent imaging to expose involvement of other organs.

An echography and MRI of the heart were conducted to reveal possible restrictive pericarditis or heart infiltration. No focal myocardial lesions were found. The increased myocardial extracellular volume suggested a slight diffuse myocardial fibrosis, but this could be caused by edema as well. Clinical significance of these findings was unclear.

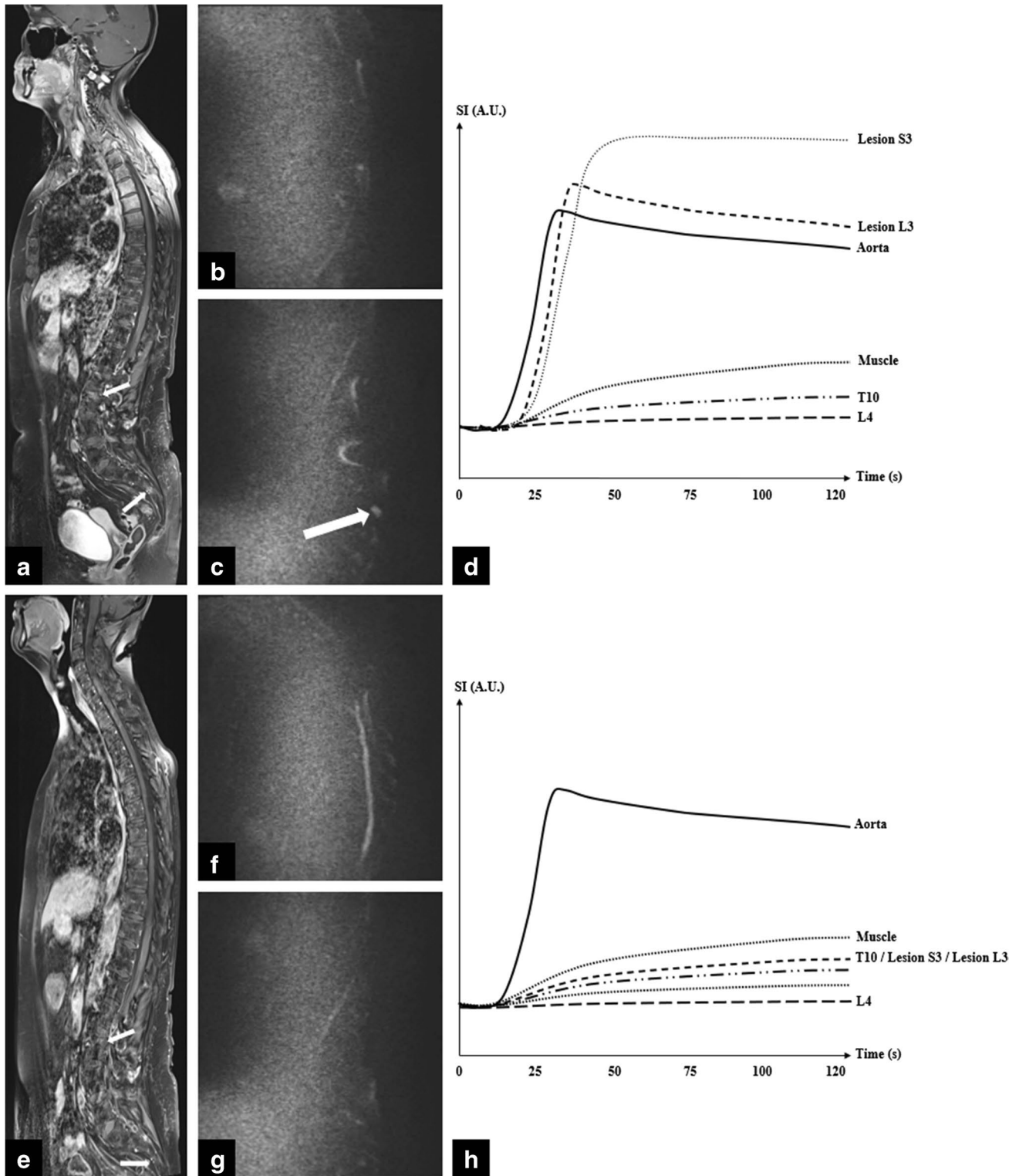
An ^{18}F -FDG-PET-CT was conducted to investigate retroperitoneal fibrosis and involvement of other organs. Two mildly to moderately active foci were observed in the upper mediastinum: one at the aortic arch and one at the base of the brachiocephalic trunk. These foci were suggestive for vasculitis caused by ECD. Other active foci were found in the axial and peripheral skeletons and matched those found in the previous ^{18}F -FDG-PET-CT.

A bone scintigraphy with technetium 99m-methyl diphosphonate (Tc-99m MDP) was performed to further investigate bone involvement. Increased bone conversion was seen in the same regions as those earlier identified. The lesions in the spine that were identified with whole-body MRI were not visible on scintigraphy. A brain MRI showed a normal adeno- and neurohypophysis. No other significant lesions were detected.

The patient was referred to the oncology department for treatment. Because of the *BRAF* mutation, treatment with dabrafenib (Tafinlar) and trametinib (Mekinist) was indicated [3, 6]. Both dabrafenib and trametinib are small molecules, inhibiting the activity of *BRAF* and *MEK*, respectively. Oral treatment was started with 2×150 mg of dabrafenib and 1×2 mg of trametinib daily.

Three months after initiation of therapy, a control ^{18}F -FDG-PET-CT scan and whole-body MRI were conducted. ^{18}F -FDG-PET-CT was conducted 60 min after intravenous ^{18}F FDG injection. The osteolytic lesions in the skeleton which were identified and characterized in the previous examinations all showed a clear decrease in metabolic activity, as well as a decrease in different osteolytic components, mainly in the right scapula and right iliac bone. The hypermetabolism at the base of the brachiocephalic trunk, which was identified in the previous examination, had completely disappeared as well. The active focus at the aortic arch (i.e., base of the subclavian artery) was still visible and showed no change in activity.

For the whole-body MRI, the protocol consisted of coronal T1- and T2-STIR-weighted images and sagittal T1-weighted, T2-weighted with fat saturation and contrast-enhanced T1-weighted images with fat saturation of the thoracic and lumbar spines, DWI and DCE-MRI. The DCE-MRI was performed in the sagittal plane (7.5 ml Gadovist bolus, arrival time 7.14 s, 20 ml saline flush) and qualitative, semi-quantitative and quantitative analyses were conducted using the same regions of interest with calculation of the TIC, wash-in, wash-out, time-to-peak, the positive enhancement integral and the iAUC. The Tofts pharmacodynamic



model was applied to calculate K_{trans} , K_{ep} , V_e and $iAUC$ (Table 3). A pixelwise T1 protocol and slow arterial input function type ($\chi^2 = 0.033$) were used.

On the anatomical sequences, a good therapy response was observed. The active bone marrow lesions identified at

diagnosis all showed significant therapy changes, resulting in an evolution of the skeletal score from 12/13 to 0/13. All smaller marrow lesions had completely disappeared and the larger lesions showed volume reduction and serous transformation with unclear, irregular borders and/or fatty infiltration

Fig. 4 Sagittal whole-spine contrast-enhanced T1-weighted images after fat saturation (**a**, **e**), sagittal thoracolumbar (thoracic vertebra 1–lumbar vertebra 3; 319×319), and lumbosacral (thoracic vertebra 11–sacral vertebra 5; 319×319) spine 3 scan trace DWI b1000 images (**b**, **c**, **f**, **g**) and dynamic contrast-enhanced MRI time-intensity curves before and after treatment (**d**, **h**). Sagittal whole-spine contrast-enhanced T1-weighted image after fat saturation before treatment (**a**) shows enhancing lesions in the L3 and S3 vertebral bodies (arrows), which show a type III (S3) curve with a plateau phase and type IV (L3) curve with steep wash-out and a rapid slope on the time-intensity curve data point fit lines of the dynamic contrast-enhanced MRI sequence (**d**) (temporal resolution 1 image/1.5 s with a total acquisition time of 117.5 s after gadolinium injection). This is indicative of high perfusion and vascularization, high bulk water flow, high vascular permeability and small interstitial space volume. The T10 and L4 vertebral bodies show no increased enhancement with flat type II (T10) and I (L4) curves indicative for localized disease. Spine 3 scan trace DWI b1000 images (**b**, **c**) only show a lesion with diffusion restriction in the S3 vertebral body (arrow). Sagittal whole-spine contrast-enhanced T1-weighted image after fat saturation after treatment (**e**) shows no enhancement in the prior lesions in the L3 and S3 vertebral bodies (arrows), which now both show a type II curve (**h**), indicative of an evolution from high perfusion with minimal to low vascular resistance and small interstitial space to low perfusion with high vascular resistance and low permeability. Spine 3 scan trace DWI b1000 images after treatment (**f**, **g**) show no pathological diffusion restriction. The identified lesion in S3 with high diffusion restriction in previous DWI examination cannot be identified. A.U., arbitrary unit; L3/L4, third/fourth lumbar vertebra; S3, third sacral vertebra; s, seconds; SI, signal intensity; T10, tenth thoracic vertebra

(Fig. 6). On DWI-MRI, the earlier identified lesions with diffusion restriction had completely disappeared. No pathological diffusion restriction was identified in the entire skeleton (Fig. 4f, g). On DCE-MRI, the aorta showed a typical arterial type IV TIC with a quick enhancement, steep wash-in followed by a wash-out. The paravertebral muscles, T10 and L4 showed a type II curve with slow first pass, slow wash-in and low sustained enhancement with a higher amplitude, a type II curve with a small amplitude and a type I curve with almost no enhancement, respectively. The lesions in L3 and S3, however, showed a type II curve with slow first pass, slow wash-in and low sustained enhancement similar to that in T10 instead of the earlier identified active type IV curve with steep first pass, rapid wash-in and steep wash-out and type III curve with steep first pass, rapid wash-in and a plateau phase with sustained enhancement. This indicates evolution from high perfusion with minimal to low vascular resistance and small interstitial space to low perfusion, high vascular resistance and low permeability (Fig. 4h).

Discussion

We report a unique description of bone lesions in ECD, with DWI and DCE-MRI. We found distinct characteristics that may help to discriminate the etiology of bone lesions, primarily between bone metastasis, MM and ECD.

Furthermore, this is the first case report with repeated ^{18}F -FDG-PET-CT and (functional multiparametric) DWI and DCE-MRI images on treatment with *BRAF* and *MEK* inhibitors in ECD. After three months of treatment, the earlier identified osteolytic lesions on ^{18}F -FDG-PET-CT all showed a decrease in metabolic activity, indicating good therapy response. This was confirmed on whole-body MRI: on anatomical sequences, active bone marrow lesions that were identified before therapy now all showed a significant necrotic, fatty or gelatinous transformation. Smaller marrow lesions had completely disappeared and the larger lesions showed volume reduction with serous transformation. On DWI-MRI, earlier identified lesions with diffusion restriction had completely disappeared after treatment. Evaluation of the DCE-MRI sequences showed that the lesions in L3 and S3 now showed a type II curve with slow first pass and low amplitude, indicating evolution from high perfusion with minimal to low vascular resistance and small interstitial space to low perfusion, higher vascular resistance and lower permeability. When the semi-quantitative and quantitative parameters obtained after therapy are compared to those obtained before therapy, it can be noted that the wash-in values in the lesions have decreased after therapy. This indicates fewer inflow, capillary leak and permeability within the lesions. Furthermore, an increase in wash-out was seen, indicating that the interstitium within the lesions expanded. The time-to-peak value increased, meaning that the histological bone marrow invasion and bone marrow perfusion diminished. The positive enhancement integral and iAUC from the TIC both decreased as well. The volume transfer constant from plasma to extravascular extracellular space (K_{trans}) decreased, indicating a decrease in exchange between blood and bone marrow. The rate constant from extravascular extracellular space to plasma (K_{ep}) increased within the L3 lesion and decreased within the S3 lesion. The extravascular extracellular space volume per unit of tissue volume (V_e) increased within the vertebral bodies and decreased within the lesions. This indicates an increase in interstitial space within the vertebral bodies and a decrease in interstitial space within the lesions. The initial area under curve from the time-concentration curve decreased.

For these reasons, a multiparametric MRI investigation of patients with ECD could provide important additional information not obtained from other imaging modalities, aiding clinicians to correctly diagnose ECD and start correct treatment in an early stage of disease.

ECD is a rare type of non-Langerhans cell histiocytosis that was first described in 1930 by J. Erdheim and W. Chester. The disease has recently been recognized as a clonal myeloid neoplastic disorder owing to the discovery of repeated mutations in the mitogen-activated protein kinase (*MAPK*) pathway [2, 11]. The disease typically affects adults between the fifth and seventh decade with a

Table 2 (Semi-)quantitative analysis of the DCE-MRI examination before therapy: Descriptive parameters of the time-intensity curve and time-concentration curve are compared between the lesions (lesion in L3 and S3) and reference tissues (aorta, paravertebral muscle, T10 vertebral body and L4 vertebral body)

	Aorta	Muscle	T10	L4	Lesion L3	Lesion S3
Time-intensity curve parameters						
Wash-in	2.069	0.157	0.005	−0.011	0.195	0.349
Wash-out	−0.107	0.012	−0.004	0	−0.009	−0.016
Time to peak	0.205	0.538	0.615	0.231	0.333	0.538
Positive enhancement integral	0.494	0.094	0.007	0.004	0.122	0.157
Initial area under curve	0.332	0.054	0.003	0.001	0.065	0.103
Time-concentration curve parameters						
Ktrans	4	0.705	0.541	0.008	3.864	4
Kep	5.515	4.136	5.031	5.214	22.224	4.507
Volume of the extracellular extravascular space	0.725	0.17	0.108	0.002	0.174	0.887
Initial area under curve	1.051	0.16	0.106	0.003	0.201	0.915

Kep rate constant, *Ktrans* transfer constant, *L3* and *L4* third and fourth lumbar vertebra, *S3* third sacral vertebra, *T10* tenth thoracic vertebra

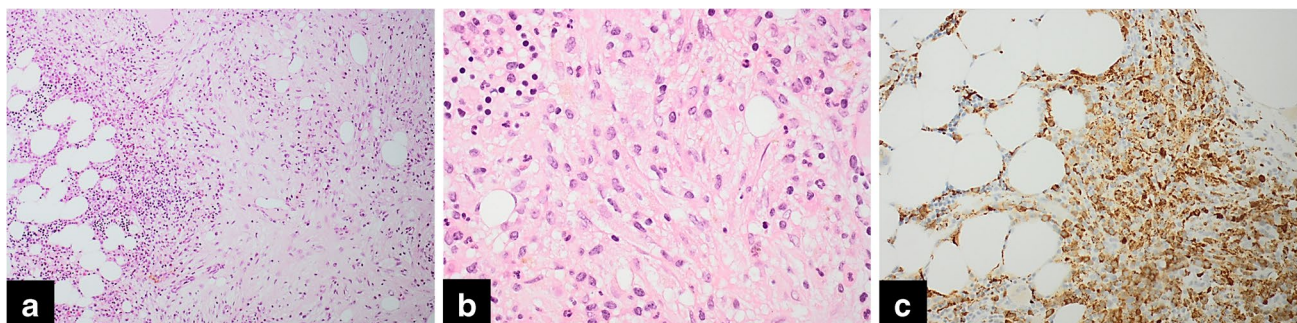


Fig. 5 Trephine biopsy of the iliac crest. **a** At low magnification, mainly fibrosis is visible (hematoxylin and eosin, $\times 100$). **b** In this case, even at high magnification, individual histiocytes are more difficult to recognize than usually in ECD, due to important fibrosis. The

background shows barely discernible histiocytes with delicate vacuolization (hematoxylin and eosin, $\times 400$). **c** At immunohistochemical staining for CD68, the histiocytes become clearly visible (hematoxylin and eosin, $\times 200$)

Table 3 (Semi-)quantitative analysis of the DCE-MRI examination after therapy: Descriptive parameters of the time-intensity curve and time-concentration curve are compared between the prior lesions (prior lesions in L3 and S3) and reference tissues (aorta, paravertebral muscle, T10 vertebral body and L4 vertebral body)

	Aorta	Muscle	T10	L4	Lesion L3	Lesion S3
Time-intensity curve parameters						
Wash-in	1.559	0.056	0	0.002	−0.01	0.076
Wash-out	−0.098	0.017	0.004	0	−0.004	0.019
Time to peak	0.205	0.923	0.641	0.256	0.718	0.718
Positive enhancement integral	0.55	0.058	0.009	0.001	0.023	0.078
Initial area under curve	0.355	0.021	0.002	0	0.004	0.028
Time-concentration curve parameters						
Ktrans	2.117	0.074	0.076	0.346	0.245	0.171
Kep	2.19	0.542	0.561	25.434	39.983	1.183
Volume of the extracellular extravascular space	0.967	0.136	0.136	0.014	0.006	0.145
Initial area under curve	1.604	0.066	0.068	0.033	0.015	0.099

Kep rate constant, *Ktrans* transfer constant, *L3* and *L4* third and fourth lumbar vertebra, *S3* third sacral vertebra, *T10* tenth thoracic vertebra

slight male predilection, affects multiple organ systems and its clinical presentation can range from asymptomatic bone lesions to multisystemic variants that are, despite being a non-malignant neoplastic disorder, potentially fatal if left untreated [12, 13]. Typical manifestations of the disease are involvement of long bones (96% of all cases) and rarely axial bones, diabetes insipidus, circumferential thickening of the aortic wall, retroperitoneal fibrosis and perinephric infiltration [14–17]. The involvement of the central nervous system is a prognostic factor and an independent predictor of fatality [1, 12, 18]. Particular histopathological findings are diffuse xanthogranulomatous infiltrations with mononuclear foamy, lipid-laden histiocytes and Touton-like polynuclear giant cells alongside the presence of lymphocytes and eosinophil infiltrations surrounded by various stages of fibrosis [13, 17–19]. Histochemical and molecular analyses of the foamy histiocytes in tissue biopsies will stain positively for CD68, CD14 and CD163 and negatively for CD1a, langerin and S100. The negative stain for CD1a is an important differential diagnostic argument to rule out Langerhans cell histiocytosis which stains positively for both CD68 and CD1a [13, 15, 17–19]. *BRAFV600E* gain-of-function mutations are present in more than 50% of the patients with ECD [1, 4, 6, 13, 18]. This recent molecular discovery alongside the recent approval of the first targeted therapy for *BRAFV600E* mutations (vemurafenib) indicates that there is a need for updated guidelines to optimize the diagnosis and treatment of ECD [3, 6]. The use of vemurafenib in patients with severe multi-systemic forms and refractory disease has been reported as highly beneficial [1, 2, 15, 16]. Other recurrent mutations were those in *NRAS*, *MAP2K1* and *PIK3CA* [18].

Imaging wise, the disease usually manifests as a bilateral symmetric cortical sclerosis accompanied by a homogenous or heterogenous sclerosis of the spongy bone typically at the diaphyseal (79%) and metaphyseal (76%) regions. The epiphyseal regions are rarely affected (8%). On MRI, the bone involvement is seen as an extensive replacement of fatty bone marrow. This results in a heterogenous low signal intensity, typically hypointense to muscle, on T1-weighted sequences, heterogenous high signal on T2-weighted sequences and heterogenous enhancement on contrast-enhanced T1-weighted sequences. The pattern of involvement is potentially related to the disease staging and can range from diffuse to geographic, nodular or reticular. MRI is particularly useful in evaluating the extent of medullary bone disease. Skeletal CT findings in ECD typically show cortical thickening and heterogenous medullary sclerosis. CT is an excellent imaging modality to investigate the presence of extraskeletal manifestations such as pulmonary involvement, cardiovascular involvement, involvement of the kidneys and/or retroperitoneum. Technetium-99 m bone scintigraphy typically shows intense bilateral symmetrical tracer uptake of the appendicular skeleton (mainly

the femur and tibia) usually sparing the epiphyseal regions. Bone scintigraphy can occasionally show increased tracer uptake in regions that were radiographically deemed normal. ^{18}F -FDG-PET-CT imaging typically reveals bilateral high ^{18}F FDG uptake in the same skeletal regions as ^{18}F accumulates inside cells that are inflammatory activated. This imaging modality also evaluates the extent of extraskeletal manifestations [17, 19–22].

Differential diagnoses of ECD based on the patient's radiological presentation include different osteosclerotic conditions such as malignant bone metastases, MM, chronic osteomyelitis, lymphoma, Paget's disease, Pyle's disease and Camurati-Engelmann's disease. Primary tumors often associated with osteolytic bone lesions are MM, renal cell carcinoma, melanoma, non-small cell lung cancer, non-Hodgkin lymphomas, thyroid cancer, breast cancer and Langerhans-cell histiocytosis. However, among these conditions, the specific extraskeletal manifestations are exclusive to ECD and its presence can rule out the aforesaid conditions. Additionally, the pattern of bone involvement that is seen on MRI can be excellent in ruling out other conditions as bone involvement in ECD typically manifests as a bilateral cortical sclerosis that is symmetric with accompanied spongy bone sclerosis sparing the epiphyseal regions [17, 19, 21].

In the case presented here, the initial clinical presentation was migratory arthralgia in the hip and knee five months after a trauma. Initial X-rays of the pelvis, right femur and right knee showed lesions suspected for osteolytic bone metastasis. In order to detect further metastases, a CT thorax and abdomen, bone scintigraphy and echography of the thyroid gland were performed. Findings on CT imaging and bone scintigraphy were suspected for malignancy, and thus, a ^{18}F -FDG-PET-CT examination was performed to identify a possible primary tumor. The bone lesions were again suspected for bone metastases, but no primary tumor was identified. A bone biopsy was taken from a lesion in the right superior posterior iliac spine. Anatomopathological examination showed an increase in polytypic plasma cells and fibrosis, but there was no evidence of metastasis. As the patient's clinical presentation was suspected for MM, a serum protein electrophoresis with immunofixation was performed, which showed no arguments of a monoclonal peak. Free light chains kappa and lambda were slightly increased but the kappa/lambda ratio was normal, indicating a polyclonal expansion. Urine protein electrophoresis showed no monoclonal peak and tumor markers were not elevated. A bone marrow sample was obtained and showed no arguments for plasma cell dyscrasias.

Whole-body MRI showed multiple focal, heterogenous bone lesions with a skeletal score of 12/13 as the left scapula remained disease free [7]. The bone lesions were non-sharply delineated and showed residual fat components, not typical for MM or metastases. DWI showed a

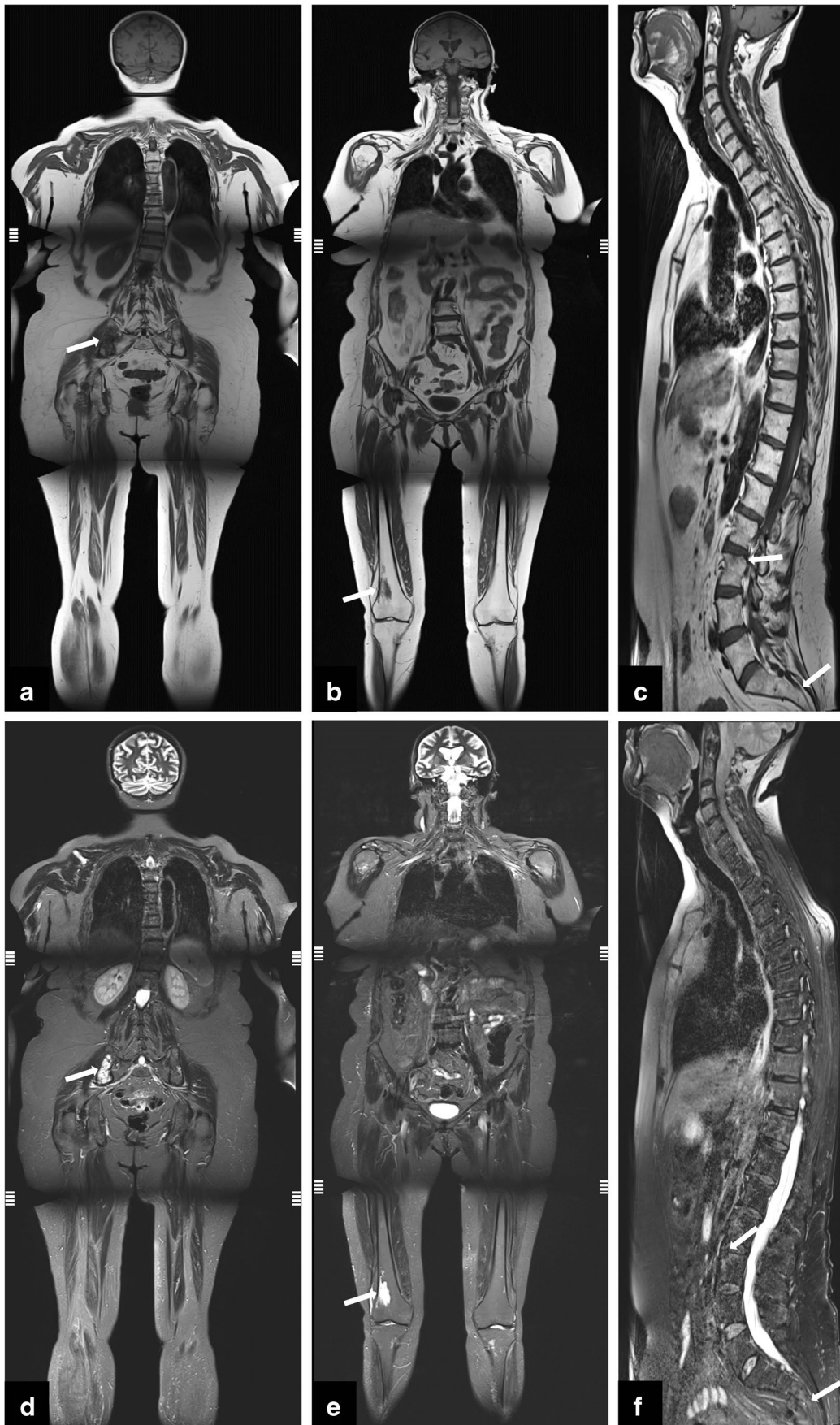


Fig. 6 Whole-body MRI examination with T1-weighted (upper row) and T2-weighted images after fat saturation (lower row) during treatment. **a, d** Coronal images show serous transformation of lesions with unclear, irregular borders in the right iliac bone (arrow). **b, e** Coronal images show serous transformation with unclear, irregular borders in the distal right femur (arrow). **c, f** Sagittal images show volume reduction in lesions of the L3 and S3 vertebral bodies (arrows)

diffusion restriction in the bone lesions, indicating dense cellular content and small interstitial space [8]. DCE-MRI of the bone lesions showed type IV curves with maximal enhancement higher than the aorta. A strong wash-in and wash-out was seen, indicating very high perfusion and minimal vascular resistance within the lesions [9]. These findings, alongside with the diffusion restriction, were consistent with focal MM lesions. The distribution pattern of the lesions however was atypical with presentation in the mandible and tibia. In MM, lesions would primarily be present in the proximal parts of the femur and humerus, pelvis, and spine [8]. Furthermore, the lesion morphology with inhomogeneous aspect, central fat inclusion and unclear irregular borders did not fit the typical presentation as seen in MM. Homogenous round lesions with a regular and clearly defined border would be typical in patients with MM and metastases [8]. Cellularity, perfusion and vascularity were not typical for MM as well. In most MM cases, there would be a diffusion restriction in the entire spine as focal lesions are mostly accompanied by diffuse bone marrow disease. In addition, the diffusion restriction would most likely be more pronounced in case of combined diffuse and focal pattern and would be present in all focal lesions [9]. The TIC of both lesions would also be a type IV curve with high wash-in and wash-out rates. Furthermore, the semi-quantitative and quantitative parameters showed differences with those found in MM, especially at the lesion found in S3. Wash-in time would be shorter and there would be stronger wash-out. The time-to-peak would also be lower [9]. The combination of results from anatomical and functional DWI and DCE-MRI sequences made it possible to exclude the diagnosis of MM. However, the heterogenous aspect of the lesions combined with the irregular borders, central fat inclusions and the distribution pattern puts up the possible diagnosis of ECD [4, 19, 20, 22]. Together with the additional findings of a small adeno- and neurohypophysis and a history of diabetes insipidus commonly associated with ECD, the diagnosis purely based on radiological presentation seemed even more likely [1]. Anatomopathological confirmation followed.

Data Availability Data (imaging and anonymized patient information from the electronic patient record) can be obtained at the data protection officer's office of the data provider (Ghent University Hospital,

Ghent, Corneel Heymanslaan 10, 9000 Ghent, Belgium), in close collaboration with the Institutional Ethical Review Board.

Declarations

Ethical approval All procedures performed in the study involving human participants are in accordance with the ethical standards of the institutional and/or national research committee and with the 1964 Helsinki declaration and its later amendments or comparable ethical standards.

Informed consent Informed consent was obtained from the subject described in this report.

Conflict of interest The authors declare no competing interests.

References

1. Haroche J, Cohen-Aubart F, Amoura Z. Erdheim-Chester disease. *Blood*. 2020;135(16):1311–8.
2. Mazor RD, Manevich-Mazor M, Shoenfeld Y. Erdheim-Chester disease: a comprehensive review of the literature. *Orphanet J Rare Dis*. 2013;8:137.
3. Goyal G, Heaney ML, Collin M, et al. Erdheim-Chester disease: consensus recommendations for evaluation, diagnosis, and treatment in the molecular era. *Blood*. 2020;135(22):1929–45.
4. Diamond EL, Dagna L, Hyman DM, et al. Consensus guidelines for the diagnosis and clinical management of Erdheim-Chester disease. *Blood*. 2014;124(4):483–92.
5. Abdelfattah AM, Arnaout K, Tabbara IA. Erdheim-Chester disease: a comprehensive review. *Anticancer Res*. 2014;34(7):3257–61.
6. Haroche J, Charlotte F, Arnaud L, et al. High prevalence of BRAF V600E mutations in Erdheim-Chester disease but not in other non-Langerhans cell histiocytoses. *Blood*. 2012;120(13):2700–3.
7. Dutoit JC, Claus E, Offner F, Noens L, Delanghe J, Verstraete KL. Combined evaluation of conventional MRI, dynamic contrast-enhanced MRI and diffusion weighted imaging for response evaluation of patients with multiple myeloma. *Eur J Radiol*. 2016;85(2):373–82.
8. Dutoit JC, Verstraete KL. Whole-body MRI, dynamic contrast-enhanced MRI, and diffusion-weighted imaging for the staging of multiple myeloma. *Skeletal Radiol*. 2017;46(6):733–50.
9. Van Den Berghe T, Verstraete KL, Lecouvet FE, Lejoly M, Dutoit J. Review of diffusion-weighted imaging and dynamic contrast-enhanced MRI for multiple myeloma and its precursors (monoclonal gammopathy of undetermined significance and smouldering myeloma). *Skeletal Radiol*. 2022;51(1):101–22.
10. Joshua DE, Bryant C, Dix C, Gibson J, Ho J. Biology and therapy of multiple myeloma. *Med J Aust*. 2019;210(8):375–80.
11. Starkebaum G, Hendrie P. Erdheim-Chester disease. *Best Pract Res Clin Rheumatol*. 2020;34(4):101510.
12. Garg N, Lavi ES. Clinical and neuroimaging manifestations of Erdheim-Chester disease: a review. *J Neuroimaging*. 2021;31(1):35–44.
13. Cives M, Simone V, Rizzo FM, et al. Erdheim-Chester disease: a systematic review. *Crit Rev Oncol Hematol*. 2015;95(1):1–11.
14. Knitz J, Kampylafka E, Wacker J, Schett G, Manger B. Erdheim-Chester disease: an important differential diagnosis and its main symptoms. *Z Rheumatol*. 2019;78(1):66–71.
15. Campochiaro C, Tomelleri A, Cavalli G, Berti A, Dagna L. Erdheim-Chester disease. *Eur J Intern Med*. 2015;26(4):223–9.

16. Munoz J, Janku F, Cohen PR, Kurzrock R. Erdheim-Chester disease: characteristics and management. *Mayo Clin Proc.* 2014;89(7):985–96.
17. Antunes C, Graça B, Donato P. Thoracic, abdominal and musculoskeletal involvement in Erdheim-Chester disease: CT, MR and PET imaging findings. *Insights Imaging.* 2014;5(4):473–82.
18. Haroche J, Papo M, Cohen-Aubart F, et al. Erdheim-Chester disease (ECD), an inflammatory myeloid neoplasia. *Presse Med.* 2017;46(1):96–106.
19. Choraria A, Andrei V, Rajakulasingam R, Saifuddin A. Musculoskeletal imaging features of non-Langerhans cell histiocytoses. *Skeletal Radiol.* 2021;50(10):1921–40.
20. Wang F, Cao X, Niu N, et al. Multisystemic imaging findings in Chinese patients with Erdheim-Chester disease. *AJR Am J Roentgenol.* 2019;213(6):1179–86.
21. Kumar P, Singh A, Gamanagatti S, Kumar S, Chandrashekhara SH. Imaging findings in Erdheim-Chester disease: what every radiologist needs to know. *Pol J Radiol.* 2018;83:e54–62.
22. Moulis G, Sailler L, Bonneville F, Wagner T. Imaging in Erdheim-Chester disease: classic features and new insights. *Clin Exp Rheumatol.* 2014;32(3):410–4.

Publisher's note Springer Nature remains neutral with regard to jurisdictional claims in published maps and institutional affiliations.

Springer Nature or its licensor (e.g. a society or other partner) holds exclusive rights to this article under a publishing agreement with the author(s) or other rightsholder(s); author self-archiving of the accepted manuscript version of this article is solely governed by the terms of such publishing agreement and applicable law.